

# Modeling of Galvanic Corrosion in three-metal Systems Consisting of ZM5 Magnesium Alloy, 6XXX Series Aluminium Alloy and 304 Stainless Steel under Thin Electrolyte Layer by Numerical Simulation, Electrochemical and Salt Spray Test

Qiangfei Hu<sup>1</sup>, Tao Zhang<sup>2,\*</sup>, Kun Hu<sup>1</sup>, Shaohua Chen<sup>1</sup>, Tianjun Diao<sup>1</sup>, Fuhui Wang<sup>2</sup>

<sup>1</sup> Anhui Province Engineering Laboratory of Advanced Building Materials, Anhui Jianzhu University, Hefei 230601, P. R. China

<sup>2</sup> Corrosion and Protection Division, Shenyang National Laboratory for Materials Science, Northeastern University, Shenyang 110819, P. R. China

\*E-mail: [zhangtao@mail.neu.edu.cn](mailto:zhangtao@mail.neu.edu.cn)

Received: 25 March 2022 / Accepted: 15 December 2022 / Published: 27 December 2022

---

Based on Ohm's law and charge conservation law and taking the polarization curves of the materials as the boundary conditions, the galvanic corrosion of a communication equipment in atmospheric environment is calculated and analyzed by numerical simulation, which is consistent with the salt spray test result. The effects of thin electrolyte layer thickness and coating damage factor on galvanic corrosion are evaluated, the corrosion mechanism of communication equipment is analyzed, and the corresponding anti-corrosion strategy is put forward.

---

**Keywords:** Communication equipment; Galvanic corrosion; Numerical simulation; Salt spray test

## 1. INTRODUCTION

Magnesium and its alloys are the most potential lightweight metal structural materials due to their low density, high specific strength and stiffness. At the same time, magnesium alloy also has the advantages of good die-casting performance, electromagnetic shielding performance, electrical and thermal conductivity, damping performance, biocompatibility and easy recovery. These excellent properties of magnesium alloys show a bright application prospect in communication electronic industry [1-4]. However, poor corrosion resistance of magnesium alloys is an important disadvantage. More seriously, magnesium alloys have a strong tendency of galvanic corrosion. Galvanic series is an important tool to judge galvanic corrosion tendency, which is the sequence of self-corrosion potential of metals in a specific medium. It can be seen from the galvanic series that magnesium alloy is the metal

material with the most negative self-corrosion potential [5]. Therefore, when contacting with other metal to form a galvanic couple in an electrolyte solution, magnesium alloy always acts as the anode of the galvanic couple, corrosion rate is accelerated compared with uncontacted with other metals. But magnesium alloy parts of communication equipment generally are need to be applied connecting with other metal parts, such as aluminum alloy and steel. Many studies have shown that galvanic corrosion of magnesium alloys contacting with other metals is very serious [6-24]. Jia [10,11] and Shi [17] revealed that a peak anodic current density for Mg-steel couple exceeded  $0.1 \text{ A/cm}^2$ , and even in Stenta's research [8] it reached  $0.13 \text{ A/cm}^2$ . Deshpande [5,18] reported that the maximum corrosion rate of Mg-steel couple reached 210 mm/a. King's results [19] showed a peak current density of about  $0.2 \text{ A/cm}^2$  for Mg-Al 2024 couple.

The common experimental methods of galvanic corrosion contain polarization curve superposition technique based on mixed potential theory [8,20-22], zero resistance ammeter technique [10-14], scanning vibrating electrode technique [18,25-27], scanning Kelvin probe technique [28,29] and scanning electrochemical microscope [30,31]. The polarization curve superposition technique is the superposition of the cathodic polarization curve of the galvanic cathode and the anodic polarization curve of the anode. The galvanic potential and current density can be obtained from the intersection point. This method gives only a theoretical average galvanic current value. Zero resistance ammeter technique can force the potential difference between galvanic anode and cathode to be zero, and measure the current flowing between the electrodes at the same time. Both polarization curve superposition technique and zero resistance ammeter technique obtain a total galvanic current without considering the influence of geometric factors and solution resistance et. al. Obviously, galvanic corrosion is not well characterized by these two techniques. From zero resistance ammeter technique, scanning Kelvin probe technique and scanning electrochemical microscope, corrosion interface information and surface potential or current density distribution can be obtained, but these methods are for small-size and simple galvanic couples. It is impossible to carry out research on large structures with complex geometry. Fortunately, with the development of computer science and technology, numerical simulation is gradually applied to the field of galvanic corrosion [5,7-9,11,32-34]. Numerical simulation method not only overcomes the shortcomings of the above experimental methods, but also shortens the experiment cycle and cost.

A communication equipment, called remote radio unit, contains four modules, which realizes the modulation and demodulation of baseband signal, digital up and down conversion technology, digital-to-analogue conversion, and converts baseband signal at intermediate frequency into radio-frequency signal. The converted radio-frequency signal is amplified and filtered and transmitted through the antenna port [35,36]. Communication equipment is used later to refer to the remote radio unit. The communication equipment is composed of magnesium alloy shell, aluminum alloy shell and stainless steel bolts shown in Fig. 1(a1, b1, c1, d1), which is equipped in the mobile communication base station.

It is in service under atmospheric environment. Due to the electrical performance requirements, each metal part needs to be electrically connected with each other. All surfaces except the contact surface between metals shall be coated in order to obtain better corrosion resistance. Theoretically, if the coating can maintain an outstanding protective effect and corrosive medium cannot enter the contact interface between the magnesium alloy and the coating through the coating barrier, the magnesium alloy should not be corroded. However, in actual service, due to the defects such as porosity or damage of the coating

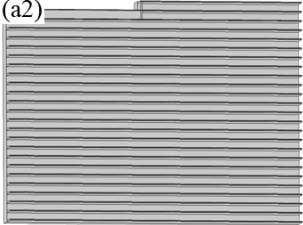
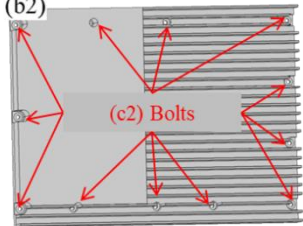
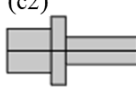
itself, the protective effect will deteriorate during the service of coating. Then corrosive medium will gradually invade, and the metal will finally corrode. Because aluminum alloy shell and stainless steel bolts are in contact with magnesium alloy shell, their potential is much higher than that of magnesium alloy. Magnesium alloy will accelerate corrosion as galvanic anode, which has serious galvanic corrosion risk.

Due to the complex structure of communication equipment and high experimental cost, it is not suitable to study its corrosion problem through common methods in the laboratory. And numerical simulation method was applied to analyze and evaluate the corrosion problem of communication equipment instead. Therefore, this paper intends to use the numerical simulation method to calculate and evaluate the risk of communication equipment corrosion, and study the influence of coating on galvanic corrosion. The salt spray test is compared with the simulation results. Then, corrosion process and mechanism are analyzed, and the corresponding protection strategies are put forward.

## 2. MATERIALS AND METHODS

### 2.1 The structure of the communication equipment

The communication equipment consists three parts, a ZM5 magnesium alloy (abbreviated as Mg) shell, a 6XXX series aluminum alloy (abbreviated as Al) shell and twelve 304 stainless steel (abbreviated as St) bolts. The geometric modeling for finite element numerical calculation is carried out according to the ratio of real object and geometric model 1:1. In order to simplify the calculation, the local details of geometric part are ignored, as shown in Fig. 1(a2,b2,c2,d2).

	Physical geometry	simplified geometric model for numerical simulation
Magnesium alloy shell	(a1) 	(a2) 
Aluminium alloy shell	(b1) 	(b2) 
Stainless steel bolts	(c1) 	(c2) 

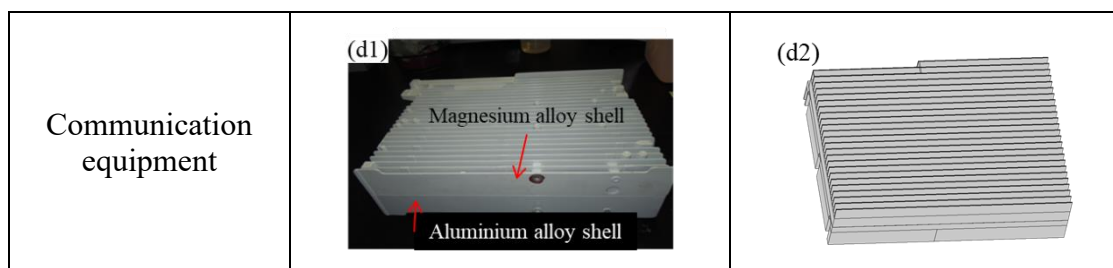


**Figure 1.** Actual shape and simplified geometric model of main components of communication equipment.

### 2.2 Potentiodynamic polarization test

In order to carry out numerical calculation later, boundary conditions must be set, that is, the polarization curves of the communication equipment materials in solution. The polarization data of various materials of communication equipment were obtained through experiments. The solution temperature was room temperature, electrolyte was 3.5 wt.% NaCl solution. All electrochemical experiments applied the classic three electrode system, composed of saturated calomel reference electrode, platinum sheet electrode and working electrodes of communication equipment materials. The Zahner electrochemical workstation was applied for electrochemical testing, the potential scanning rate was 0.333 mV/s. In order to obtain a wide enough scanning range, the cathode and anode branches were scanned respectively and then combined together. Before the test, the system was stabilized for 5 minutes to reach a relatively stable open circuit potential. For better repeatability, the experiments were repeated more than three times.

### 2.3 Mathematical model of the communication equipment galvanic corrosion in atmospheric environment

There are many articles on the numerical simulation of galvanic corrosion, but most of them are calculated when the galvanic couple is in thick electrolyte solution [8-11, 15-19], rather than when there is only a thin electrolyte layer on the surface of the galvanic couple, for example, corrosion in atmospheric environment.

Of course, the modeling of galvanic corrosion under thin electrolyte layer can be the same as that in thick electrolyte solution, mainly to solve the potential and current distribution in thin electrolyte layer. However, because of the complex geometric structure of the couple surface, the difficulty of geometric modeling and solution of thin electrolyte layer will increase. For the thin electrolyte layer, if the potential change in the normal direction of the boundary can be ignored, the original solution of partial differential equations in the three-dimensional electrolyte domain is simplified to the electrolyte charge transport in the thin electrolyte layer in the tangential direction of the boundary, which can avoid the potential problem of mesh anisotropy in the thin electrolyte layer [7,37-38].

Over the thin electrolyte domain in Fig. 2 (over the exterior surfaces of the communication

equipment), the electrolyte potential  $\phi_l$  satisfies the Ohm's law (Eq. (1)) [7,37-38]. It is used in conjunction with charge conservation law (Eq. (2)) to describe current transmission in thin electrolyte layer [7,37-38].

$$\mathbf{i}_l = -\sigma \nabla_T \phi_l \tag{1}$$

$$\nabla_T \cdot (d \mathbf{i}_l) = 0 \tag{2}$$

where  $\mathbf{i}_l$  (unit: A/m<sup>2</sup>) is the electrolyte current density vector,  $\nabla_T$  the tangential gradient operator,  $d$  (unit: m) the electrolyte layer thickness and  $\sigma$  (unit: S/m) the electrolyte conductivity.

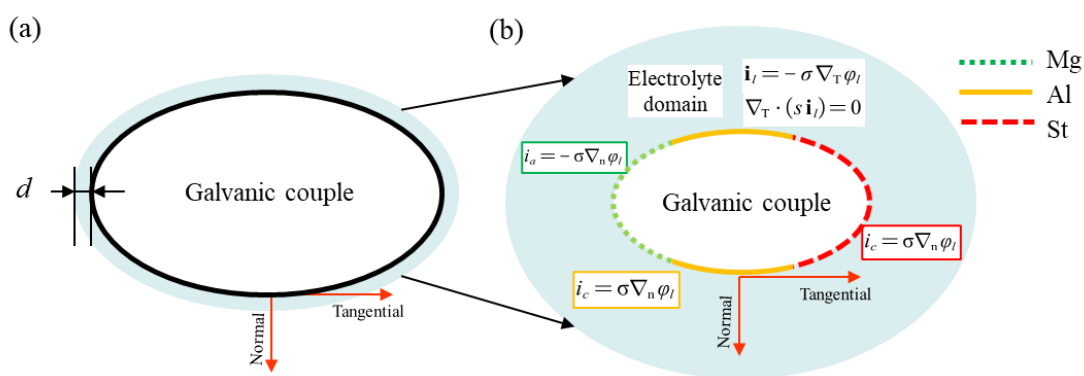


**Figure 2.** Governing equation and boundary conditions of thin electrolyte layer.

For the interface without reaction, the insulation condition is set and the current density is equal to zero. For the interfaces where the reaction occurs at the cathode and anode surface, the boundary conditions are the corresponding cathodic polarization curve and anodic polarization curve, respectively. It is assumed that there are only anodic corrosion on the anodic metal and only cathodic reaction on the cathodic metal. Relationship between current density ( $i$ ) and potential ( $\phi_l$ ) of anode and cathode (symbolized as  $a$  and  $c$ ) are displayed in Eq. (3) and Eq. (4) as [39].  $i_a$  or  $i_c$  is the current density flowing throughout the surface of the anode or the cathode in the normal direction ( $n$ ), respectively. All corrosion numerical simulations are completed by COMSOL Multiphysics software.

$$i_a = -\sigma \nabla_n \phi_l \tag{3}$$

$$i_c = \sigma \nabla_n \phi_l \tag{4}$$

#### 2.4 Boundary conditions for numerical simulation of galvanic corrosion

Communication equipment is composed of three materials. Due to their different corrosion potentials, there is a risk of galvanic corrosion. All polarization curves are shown in Fig. 3, and relevant polarization parameters are displayed in Table 1. In Fig. 3 it is depicted that the corrosion potential (0.058 V) of St bolt is the highest, that of Mg shell (-1.362 V) is the lowest, and that of Al shell (-0.051 V) is in the middle. Corrosion current densities of St bolt, Al shell and Mg shell are 0.3, 0.9, 20.8  $\mu\text{A}\cdot\text{cm}^{-2}$ ,

respectively. According to the mixed potential theory and boundary conditions, St bolts and Al shell are the cathode, and Mg shell acts as the anode of the galvanic couple.

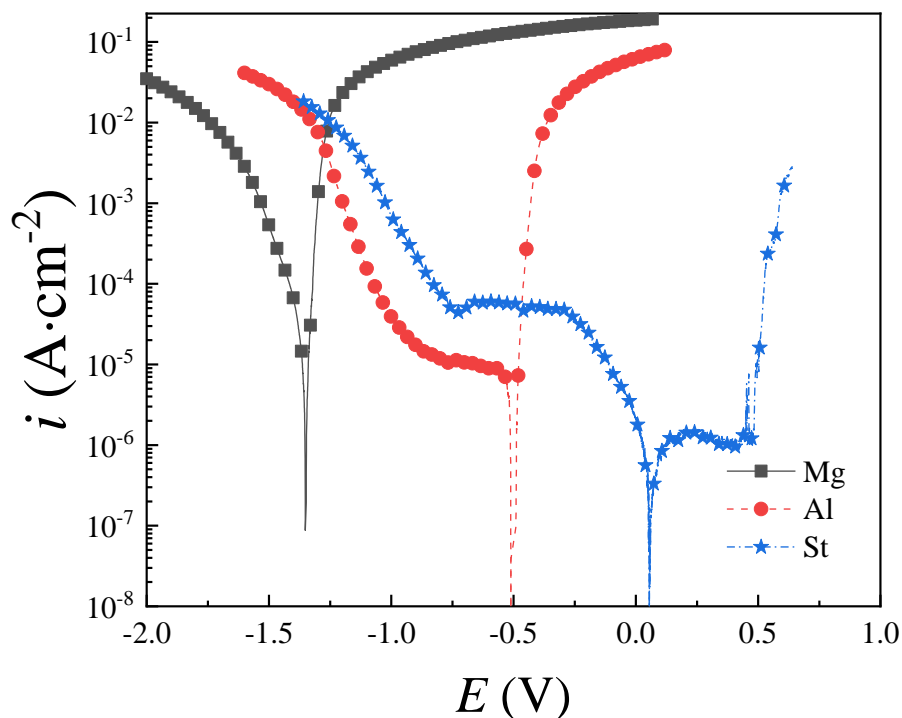


**Figure 3.** Polarization curve of communication equipment materials in 3.5% sodium chloride solution.

**Table 1** Parameters of potentiodynamic polarization curves for communication equipment materials.

Materials	Corrosion potential (V)	Corrosion current density ( $\mu\text{A}\cdot\text{cm}^{-2}$ )
Mg	-1.352	20.8
Al	-0.511	0.9
St	0.058	0.3

### 2.5 Meshing

According to the characteristics of galvanic corrosion, the corrosion is the most serious at the material junction, which needs to be paid attention to, so the mesh division at the junction is very fine. It included the adjacent region of Mg shell and Al shell (red solid line rectangular region in Fig. 4(a)) and the adjacent region of St bolt and Al shell (red dotted line circle area). Free triangular mesh was used. The maximum and minimum cell sizes were 2.26 and 0.0347 mm, respectively. The maximum cell growth rate was 1.05 and the curvature factor was 0.2. The rest of the grid was coarse, the maximum and minimum cells were set to 40 and 7.2mm, respectively, the maximum cell growth rate was 1.5 and the

curvature factor was 0.6. The total number of triangular meshes was 154256, and the average mesh quality of triangle was 0.75, which was evaluated by skewness. The grid quality distribution is shown in Fig. 4(b). When the legend color changed from red to green, the grid quality increased from 0 to 1. This division choice was to ensure the calculation accuracy and reduce the amount of calculation at the same time.

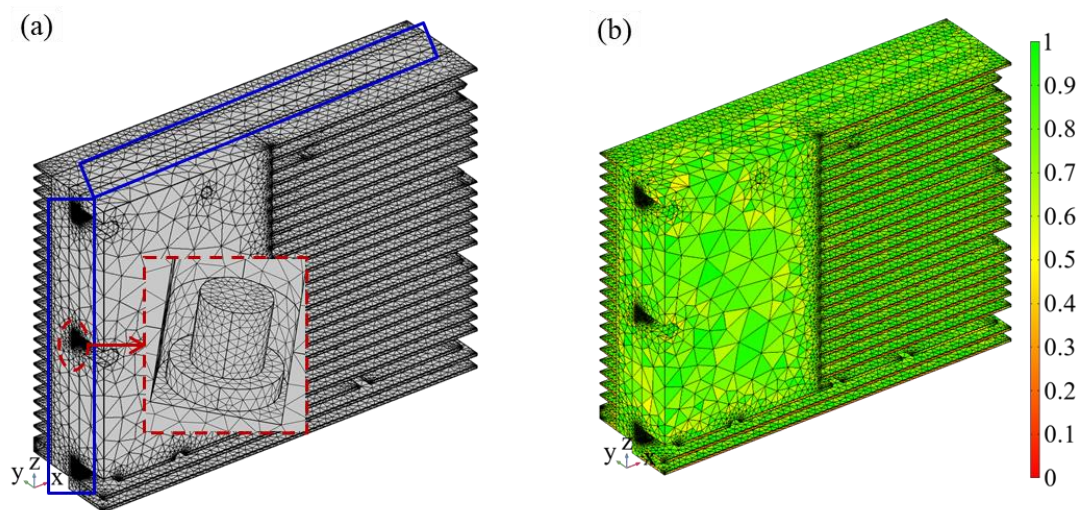


**Figure 4.** Grid division results of communication equipment (a) and cloud map of grid quality distribution (b).

## 2.6 Salt spray test

The neural salt spray test is carried out according to the American salt spray test standard (ASTM b117-03). The communication equipment is assembled first, then sprayed with coating, and finally put into the salt spray test chamber. Take it out after 720 hours, observe and take photos. The salt spray test chamber maintains a temperature of 35°C and a corrosion medium of 5 wt.% NaCl solution. A continuous spray method is adopted.

## 3. RESULTS AND DISCUSSIONS

### 3.1 Simulation results of galvanic corrosion of communication equipment

#### 3.1.1 Effect of electrolyte layer thickness

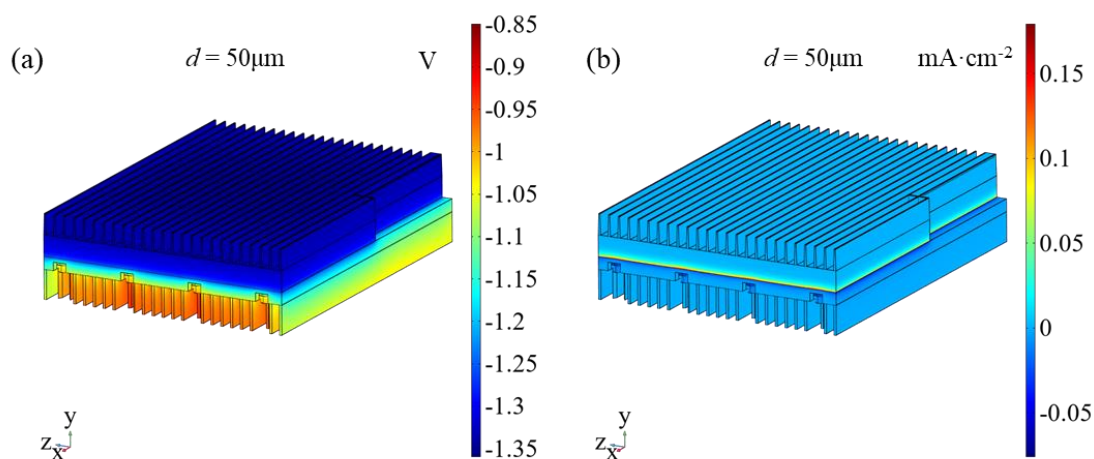
Generally, in atmospheric environment, the thickness of electrolyte layer will be less than 1mm [40]. Therefore, three thicknesses of 0.05 mm, 0.2 mm and 0.5 mm are selected to calculate the distributions of galvanic corrosion potential and current density of communication equipment through numerical simulation, shown in Fig. 5, where the coating damage coefficient is very small, and set to

0.01 [41]. In order to compare the distribution of potential and current density under different electrolyte layer thicknesses, the same color ranges are used, respectively. The potential distributions are between -1.36 and -0.85 V displayed in Fig. 5(a, c, e). The potential gradually changes from the blue end to the red end, indicating that the potential gradually increases. In comparison, the potential distributions under different layer thicknesses are basically similar. St bolt surface potential is the highest, Al shell is the second, and Mg shell is the smallest. The potential change is most obvious near the contact between Mg shell, Al shell and St bolts. In Fig. 5(b, d, f), current density changes from -0.076 to 0.179 mA·cm<sup>2</sup>. According to Eq. (5) [18], the maximum corrosion rate is about 3.91 mm/y;

$$V_L = - \frac{mi}{n \times 26.8} \times \frac{8.76}{\rho} \times 10^4 \quad (5)$$

Where, *m* is relative atomic mass (*m* = 24.3 g), *i* current density of Mg shell (A·cm<sup>-2</sup>), *n* number of electrons in electrode reaction (*n* = 2); *ρ* density of Mg shell (*ρ* = 1.82 g·cm<sup>-3</sup>).

Positive current and negative current represent anode current and cathode current respectively. In general, the current density distributions are very uniform at a far distance from the junction of different materials, and the current densities change sharply near the junction. Compared with other places, the corrosion rates of Mg shell at the junction are faster. The greater the electrolyte layer thickness, the more obvious the galvanic corrosion. This may be because the greater the thickness of the electrolyte layer, the smaller the tangential flow resistance of the current along the metal surface, the greater the current density on the surface of Mg shell, and the farther the action distance. Therefore, under 0.5 mm electrolyte layer thickness, the galvanic current at the junction is larger and changes over a wider distance, although the absolute value of galvanic action distance is still relatively small. Compared with the self-corrosion rate of Mg shell, the maximum galvanic corrosion rate of Mg shell increases by 8 times.



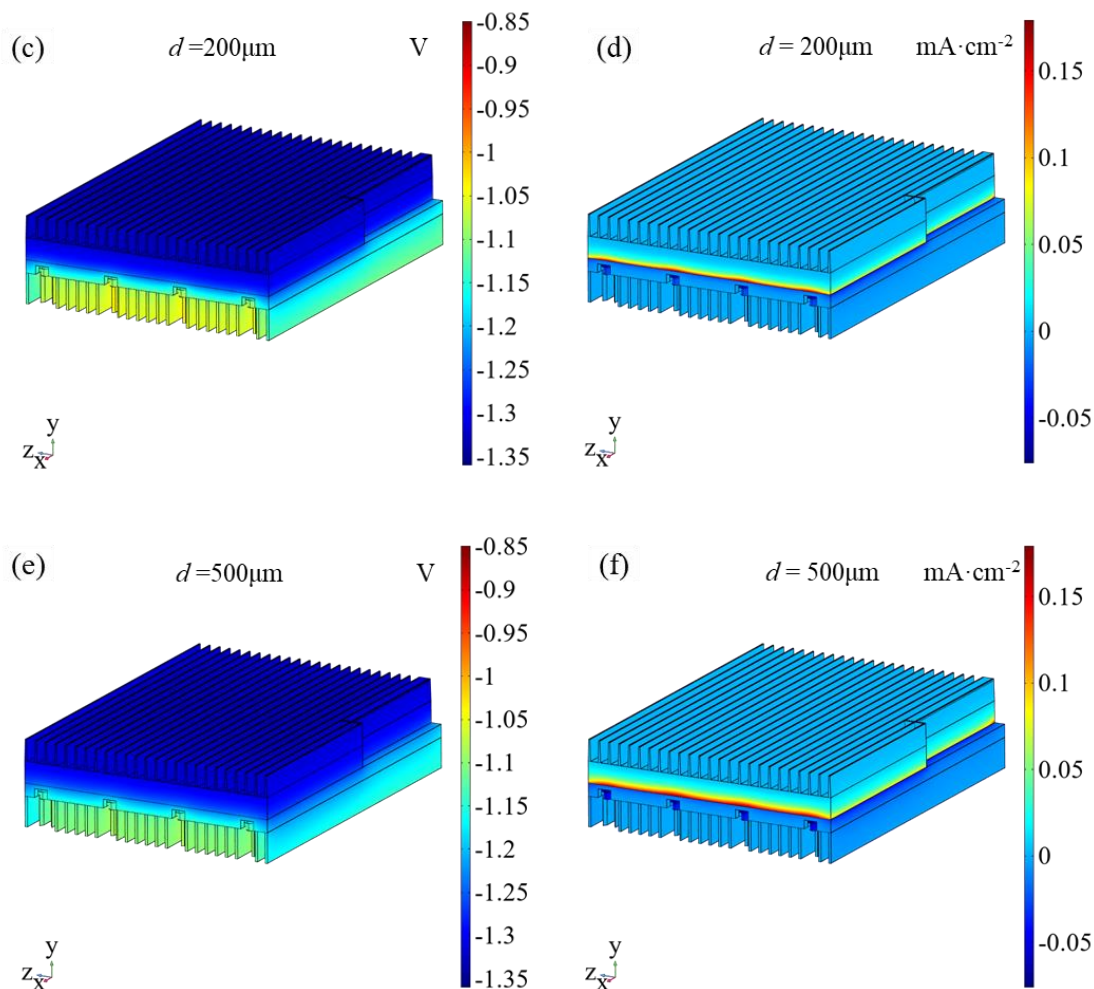


**Figure 5.** Simulation results of galvanic corrosion potential (a,c,e) and current density (b, d,f) distribution of communication equipment under different electrolyte layer thickness ( $d = 0.05, 0.2, 0.5$  mm).

It can be roughly known from the simulation results that Mg shell near the contact of the three materials of communication equipment is the most seriously corroded. In order to see the simulation results more intuitively, as shown in Fig. 6, two places, red dotted line 1 and green solid line 2, are select to calculate the potential distribution and current density distribution results, respectively. Both of them are lines in the  $z$ - $o$ - $y$  plane and the  $x$ -axis coordinate is 0 mm. Red dotted line 1 is a straight line parallel to the  $z$  axis with  $y = 0$  mm, and  $z$  from 300 to 0 mm. Green solid line 2 is a line in the range from  $y = -15$  to  $y = 25$  mm with  $z = 0$  mm, which is parallel to the central axis of the bolt. From the potential distributions in Fig. 7(a), the shapes of potential distribution curve are similar, and the potentials reach a maximum near each bolt. With the increase of electrolyte layer thickness, the overall potential increases and the anodic polarization becomes more serious. In Fig. 7(b), current distributions of three electrolyte layer thicknesses have the same characteristic. The results are in accordance with King's research [19], where for Mg-AA2024 couple the increase of electrolyte layer thickness from  $1 \mu\text{m}$  to  $1000 \mu\text{m}$  results

in increased anodic polarization of Mg to a further distance and increased throwing power. And the potential distribution is similar to that of Stenta [8], where for a Mg-Steel couple the electrolyte layer thickness changes from 0.16 mm to 10mm.

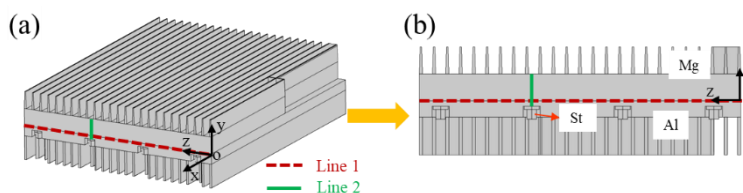


**Figure 6.** Schematic diagrams of selected section position (Line 1 and Line 2).

The corrosion current density of Mg shell near the bolt increases, while that away from the bolt decreases gradually, with the lowest on both sides. This is because the St bolt has the highest self-corrosion potential, the highest potential difference with Mg shell, and the galvanic corrosion current density is relatively higher. With the increase of electrolyte thickness, the current distribution curve moves upward, indicating that the corrosion current density increases as a whole. When electrolyte layer thickness is 0.05 mm, current density changes from 0.03 to 0.065 mA·cm<sup>2</sup>, which is about 1.5 to 3.2 times of self-corrosion current density of Mg shell. When electrolyte layer thickness raises to 0.5 mm, due to the galvanic corrosion acceleration effect, the corrosion rate of Mg shell becomes 2 to 4 times of the self-corrosion rate.

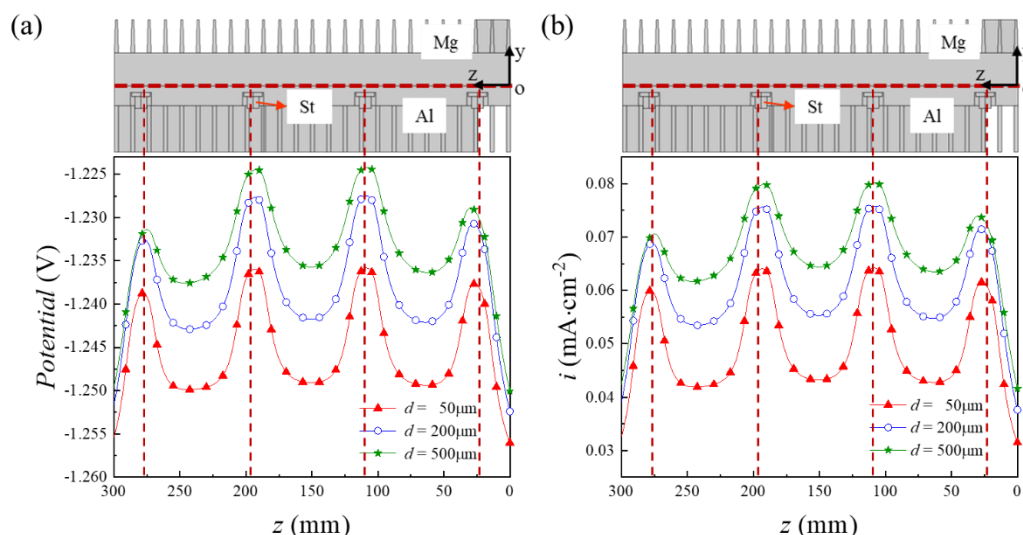


**Figure 7.** Simulation results of potential (a) and current density (b) distribution of Mg shell surface at red dotted line under different electrolyte layer thicknesses.

Simulation results of potential and current density distributions of Mg shell at green solid line under different electrolyte layer thicknesses are displayed in Fig. 8. From the potential distribution results in Fig. 8(a), the potential decreases gradually from Al shell on the left to Mg shell on the right. For 0.5 mm electrolyte layer thickness, potential drops from -1.18 V to -1.30 V. When electrolyte layer

thickness is 0.2 mm, potential gradually decreases from -1.15 V to -1.32 V. For 0.05 mm electrolyte layer thickness, potential changes from -1.10 V to -1.33 V. With the increase of electrolyte layer thickness, the potential on one side of Al shell decreases and that on one side of Mg shell increases. The potential distribution becomes more uniform. It is shown in Fig. 8(b) that the current densities on one side of the Al shell are the cathode current. Current density distributions are similar in shape. With the decrease of the distance from Mg shell, the current density increases. The anode current is on one side of Mg shell. When the distance from Al shell reduces, the current density raises. For 0.5 mm electrolyte layer thickness, the maximum current density is about 6.5 times of the self corrosion current density. In short, the closer to the junction of the two, the current density of the anode and cathode increases rapidly. With the increase of electrolyte layer thickness from 0.05 mm to 0.5 mm, the current density of anode and cathode increases, and the current attenuation speed is faster. In other words, the current density distribution is more uniform and the action distance is longer. These potential and current density distribution profiles are in agreement with Stenta's and King's results [8,19], who discussed the effect of electrolyte layer thickness on current density distribution for Mg-Steel and Mg-AA2024 couple, respectively.

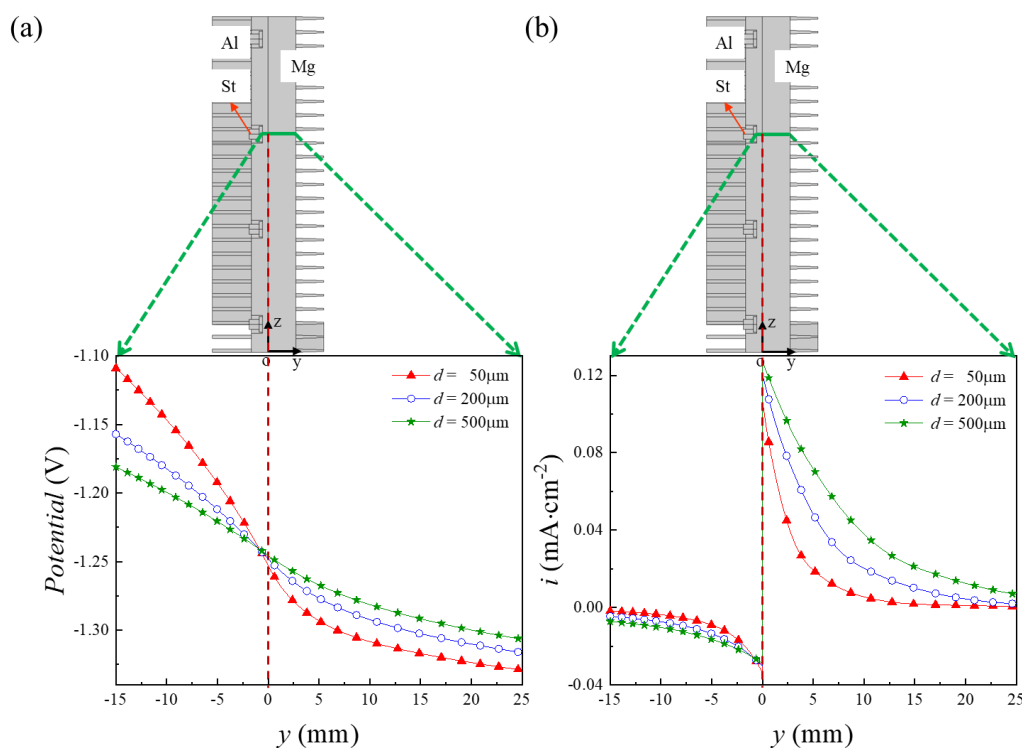


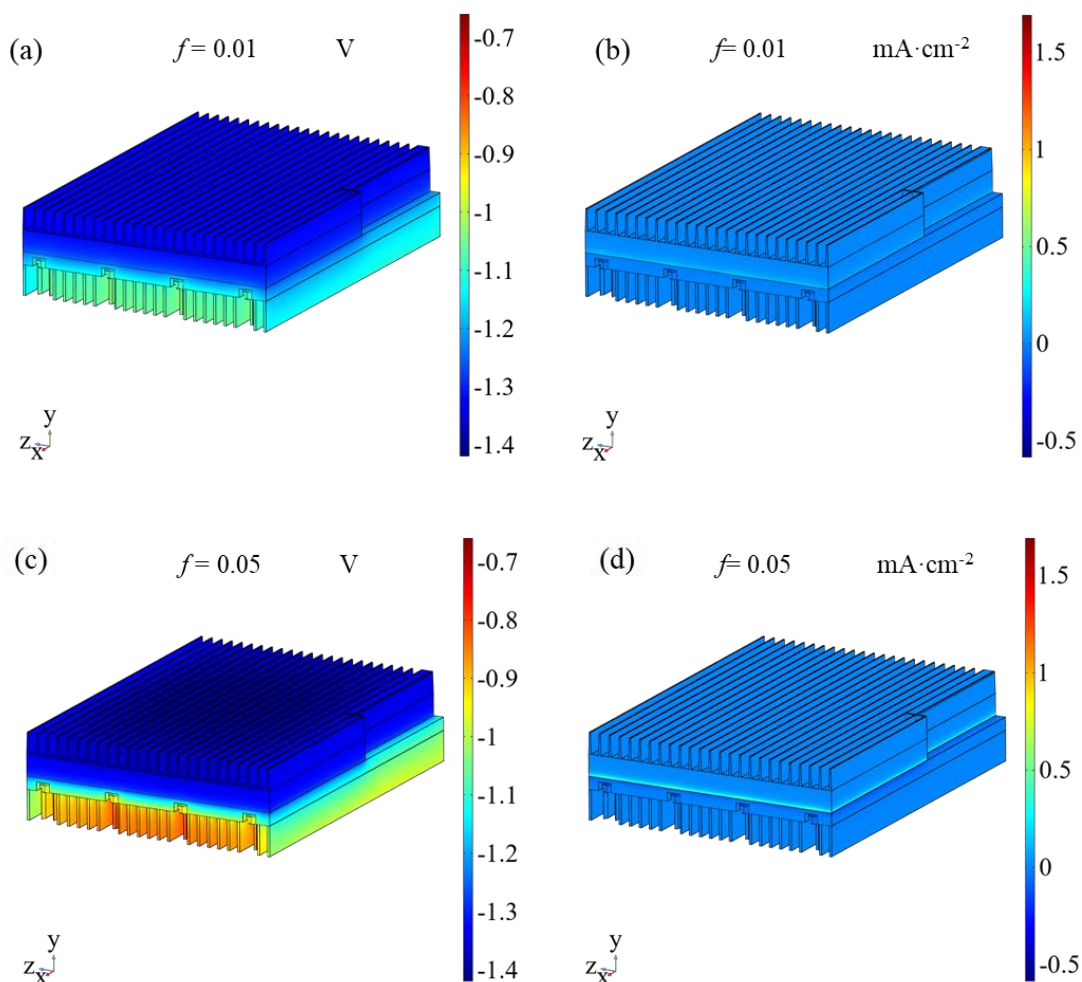
**Figure 8.** Simulation results of potential (a) and current density (b) distribution of Mg shell surface at green solid line under different electrolyte layer thicknesses.

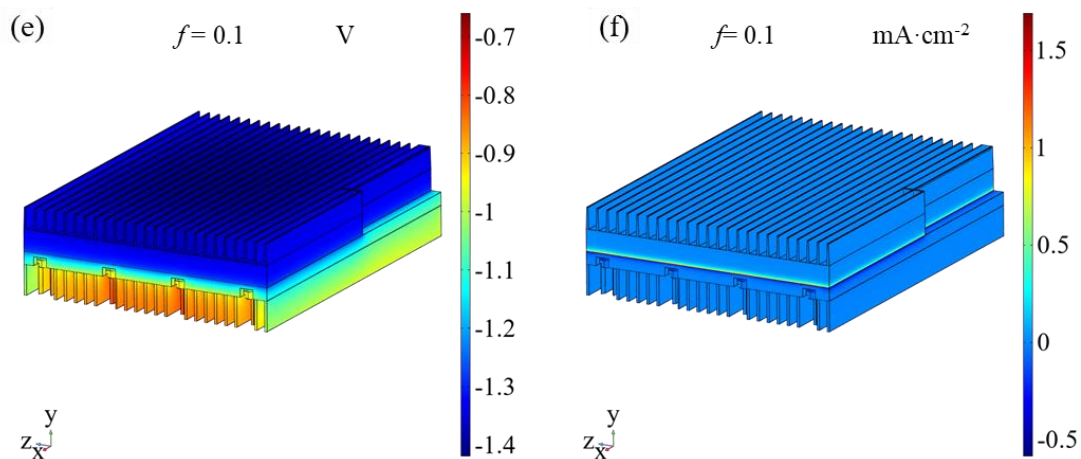
### 3.1.2 Effect of coating damage

Coating is one of the most commonly used anti-corrosion methods. The coating plays a protective

role mainly by physically isolating metal and corrosive medium. Although the ideal coating can inhibit corrosion to the greatest extent, the coating will be damaged for various reasons, so as to reduce the protection effect, in which the coating damage factor is an important parameter. The coating damage factor ( $f$ ) is the proportion of the damage area to the total area, which is a value between 0 and 1 [41,42]. The larger the coating damage factor, the larger the damage area, and the worse the protective effect of the coating. When considering the effect of coating damage, the polarization curves of uncoated metal multiplied by the coating damage factor is used as the boundary condition of galvanic corrosion numerical simulation [41].

Three values of 0.01, 0.05 and 0.1 are selected to discuss the influence of coating damage factor on galvanic corrosion of communication equipment. Simulation results of galvanic corrosion potential and current density distribution of communication equipment under different coating damage factors are displayed in Fig. 9. The color range of potential distribution diagram data is from -1.42 to -0.66 V in Fig. 9(a, c, e), and the current density range is between -0.587 and 1.69 mA·cm<sup>-2</sup> in Fig. 9(b, d, f). The maximum corrosion rate reaches 36.88 mm/y. The potential distribution and current density distribution are similar under different damage factors, respectively. Mg shell is used as anode, and the current density is positive. With the approach to the Mg shell and St bolts, the current density on the surface of the Mg shell increases rapidly and the corrosion accelerates. With the increase of coating damage factor, the corrosion rate of Mg shell surface is faster.

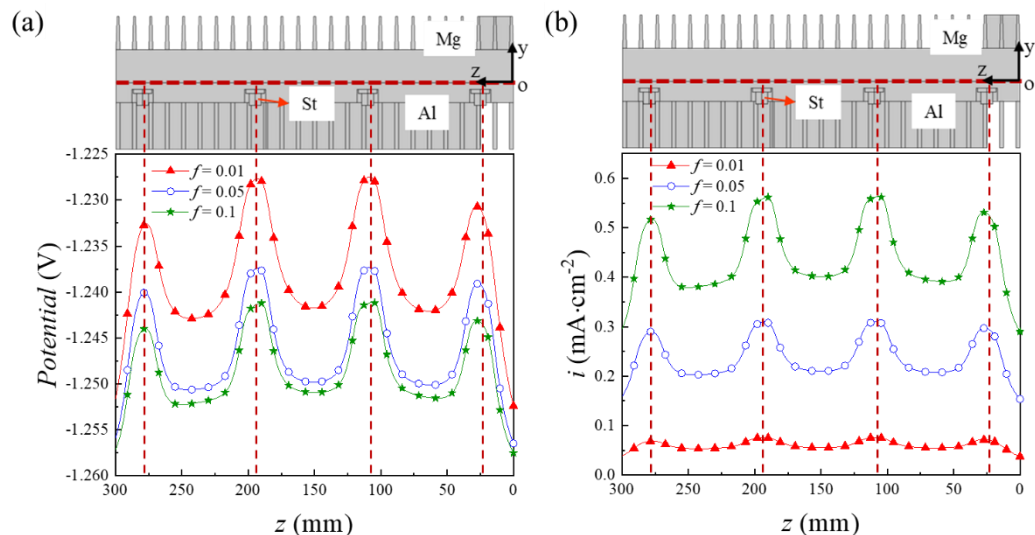




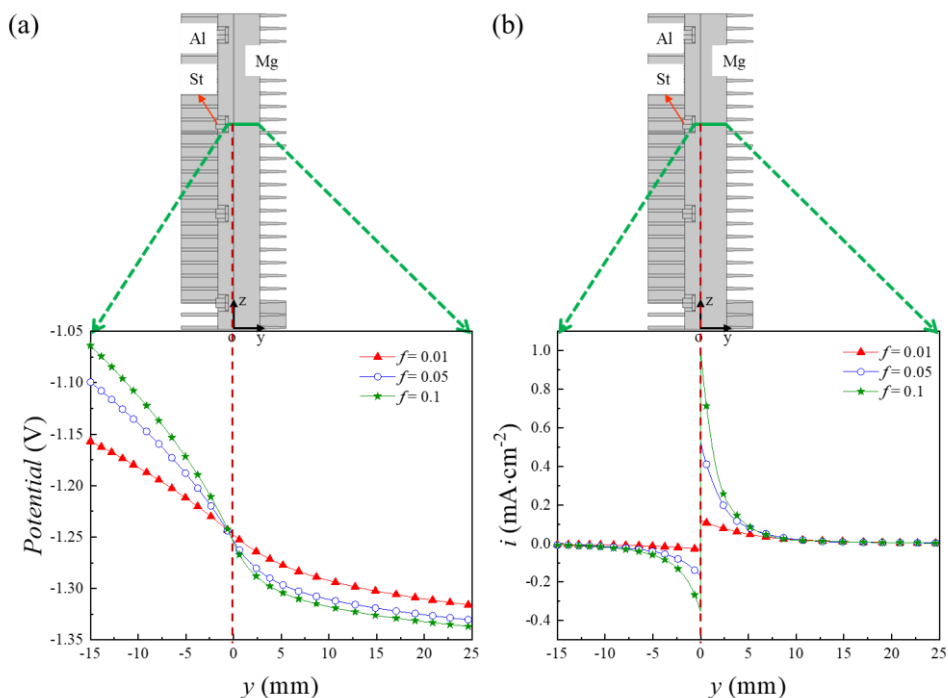
**Figure 9.** Simulation results of galvanic corrosion potential and current density distribution of communication equipment under different coating damage factors.

Fig. 10 depicts the simulation results of potential and current density distribution of Mg shell surface at red dotted line under different coating damage factors. With the increase of coating damage factor from 0.01 to 0.1, both the potential in Fig. 10(a) and current density in Fig. 10(b) increase from  $z = 0$  to  $z = 300$  mm. Near the St bolt, the potential of the Mg shell is high, which should be due to the high self-corrosion potential of the bolt, the high degree of anodic polarization to the Mg shell and the corresponding high current density. Due that only anodic dissolution reaction occurs on the metal as anode, and only cathodic reduction reaction occurs on the cathode metal. Therefore, the total surface current of Mg shell is approximately equal to galvanic current. With the increase of coating damage factor, the current density distribution on the surface of Mg shell moves up as a whole, and the total current increases. Thiel and Huber [41,43] used numerical simulation method to study the effect of coating damage factor on forced current cathodic protection, and found that the increase of damage factor increased the cathodic protection current required. According to the principles of galvanic corrosion and cathodic protection, they are essentially the same. The total galvanic current is equal to the cathodic protection current. So results are in good agreement with Thiel and Huber's results.

When the damage factor is to 0.1, the maximum current density on the surface of Mg shell is 28.5 times of the self-corrosion rate, while when the damage factor is 0.01, it is only 3.8 times of the self-corrosion rate.



**Figure 10.** Simulation results of potential (a) and current density (b) distribution of Mg shell surface at red dotted line under different coating damage factors.



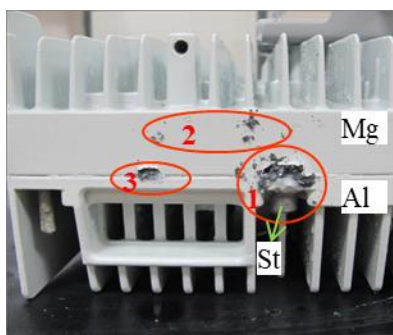
**Figure 11.** Simulation results of potential (a) and current density (b) distribution of Mg shell surface at green solid line under different coating damage factors.

Simulation results of potential and current density distribution of Mg shell surface at green solid line under different coating damage factors are shown in Fig. 11. The potential decreased gradually from  $z = -15$  mm to  $z = 25$  mm. With the increase of coating damage factor from 0.01 to 0.1, the potential distribution changes from the range from -1.154 to -1.320 V to the range from -1.058 to -1.343 V, which

is more uneven. When coating damage factor raises to 0.1, the maximum current density on the Mg shell of the solid green line increases to  $1 \text{ mA} \cdot \text{cm}^2$ , which is 500 times of self-corrosion rate of Mg shell. And the distribution of current density is relatively uneven, and the action distance of galvanic couple is shorter.

### 3.2 Salt spray test result

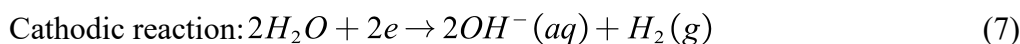
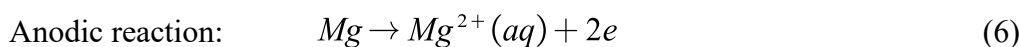
Fig. 12 is the macro photo of the surface after 720 hours of service. It can be seen that there is no corrosion trace on the aluminum alloy shell and bolts, and there is obvious corrosion on the surface of magnesium alloy, mainly near the connection between magnesium alloy and bolts (area of red circle 1), near the contact between magnesium alloy and aluminum alloy (area of red circle 2), and at the damaged coating on the surface of magnesium alloy (area of red circle 3).



**Figure 12.** Macro corrosion photos after 720h salt spray test of communication equipment.

Combined with numerical simulation results of galvanic corrosion of communication equipment and salt spray test result, corrosion mechanism of communication equipment is inferred as follows.

In the initial stage, the coating plays a good role in mechanical isolation, so the Mg shell does not corrode and there is no galvanic effect shown in Fig. 13(a). In the coating deterioration stage, corrosive medium gradually intrudes into the interface between metal and coating in Fig. 13(b), isolation effect of the coating gradually decreases, and the Mg shell corrodes. For corrosion of magnesium alloy, anodic process and cathodic process are dissolution of magnesium as Eq. (6) and hydrogen evolution as Eq. (7), respectively. Total corrosion electrochemical reaction is as Eq. (8), and corrosion product  $\text{Mg(OH)}_2$  and hydrogen generated [44-49].



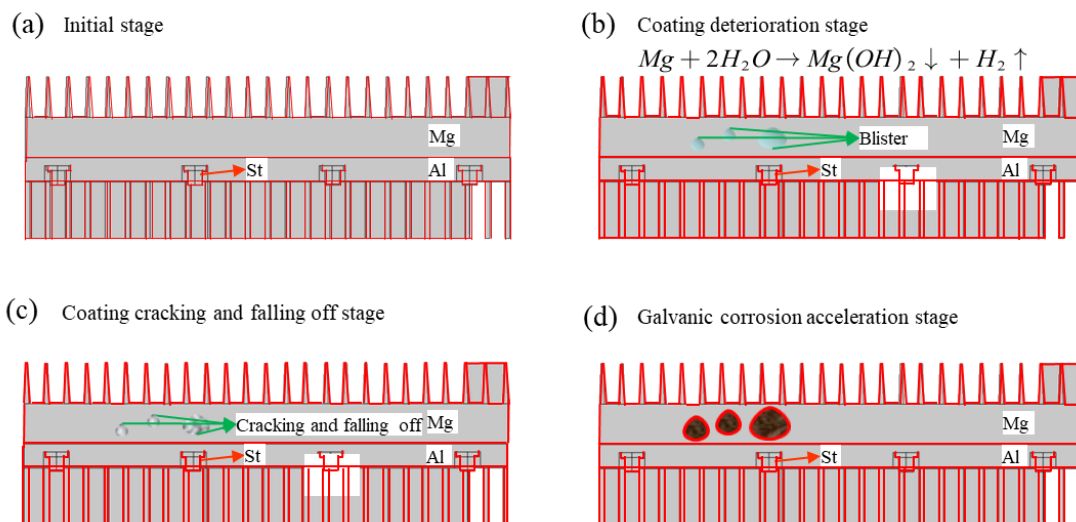


**Figure 13.** Schematic diagram of corrosion mechanism of communication equipment: (a) Initial stage; (b) Coating deterioration stage; (c) Coating cracking and falling off stage; (d) Galvanic corrosion acceleration stage.

This corrosion product layer was not able to protect the Mg shell from corrosive attack [50], the hydrogen can't overflow smoothly, and a large stress will be generated at the interface between the Mg shell and the coating. When it accumulates to a certain extent, the coating will blister (Fig. 13(b)) and crack (Fig. 13(c)) [51], and the anodic process is promoted [45]. In addition, galvanic corrosion effect of communication equipment gradually increases, and corrosion of Mg shell as an anode accelerates, especially near the Al shell and bolts, which will accelerate and lead to blistering and cracking of the coating in Fig. 13(b-c). Finally, with the damage of Mg shell coating, galvanic corrosion was further strengthened [52-54] and corrosion of Mg shell was further accelerated, resulting in corrosion failure of the whole communication equipment shown in Fig. 13(d).

From the numerical calculation and salt spray test, the overall trend of the two results is consistent. Due to the large potential difference between the constituent materials of communication equipment, the galvanic corrosion effect is very strong, especially the corrosion rate of magnesium alloy near the bolt and the aluminum alloy shell.

According to this mechanism and the simulation results of galvanic corrosion of communication equipment, the following suggestions are put forward to reduce the corrosion rate: firstly, select a better anti-corrosion coating to enhance the isolation effect of the coating and inhibit corrosion; Reduce the thickness of electrolyte layer on the surface; Replace the St bolt with material with lower potential to reduce the potential difference and reduce the corrosion rate.

#### 4. CONCLUSIONS

A communication equipment is composed of Al shell, Mg shell and St bolts, which is applied in atmospheric environment. From the perspective of numerical calculation of galvanic corrosion of communication equipment, based on Ohm's law and charge conservation law, the potential control equation in the thin electrolyte layer on the surface of communication equipment is established. Taking

the material polarization curve as the boundary condition, the distribution of potential and current density on the surface of communication equipment is solved, and the effects of thin electrolyte layer thickness and coating damage factor on galvanic corrosion of communication equipment are analyzed. The simulation results are basically consistent with the experimental results of salt spray acceleration corrosion. Based on these results, the causes of corrosion of communication equipment are analyzed, and the corresponding anti-corrosion suggestions are put forward. For galvanic corrosion of complex structures, numerical simulation provides an efficient and cost-effective way for corrosion prediction and evaluation, which has important engineering significance.

#### ACKNOWLEDGEMENTS

The authors wish to acknowledge the financial support of Natural Science Foundation of Anhui Education Department (KJ2021A0628), Anhui Jianzhu University PhD Start-up Fund (2019QDZ01), Director Fund of Anhui Province Engineering Laboratory of Advanced Building Materials (JZCL010ZZ), National Innovation and Entrepreneurship Training Program for College Students (C21006), Natural Science Foundation of Anhui Province (2008085QE274), Key Natural Science Research Project of Department of Education of Anhui Province (KJ2020A0475), Major Special Projects of Science and Technology of Anhui Province (201903a07020002), and the National Program for Support of Top-notch Young Professionals.

#### References

1. M. Esmaily, J.E. Svensson, S. Fajardo, N. Birbilis, G.S. Frankel, S. Virtanen, R. Arrabal, S. Thomas and L.G. Johansson, *Prog. Mater. Sci.*, 89 (2017) 92.
2. A. Atrens, Z. Shi, S.U. Mehreen, S. Johnston, G. Song, X. Chen and F. Pan, *J. Magnes. Alloy.*, 8 (2020) 989.
3. A. N. Alhazaa, E. Sherif and H. S. Abdo, *Int. J. Electrochem. Sci.*, 10 (2015) 5420.
4. M. E. Ikpi, J. H. Dong and W. Ke, *Int. J. Electrochem. Sci.*, 10 (2015) 552.
5. K.B. Deshpande, *Corros. Sci.*, 52 (2010) 3514.
6. J.W. Wilder, C. Clemons, D. Golovaty, K.L. Kreider, G.W. Young and R.S. Lillard, *J. Eng. Math.*, 91 (2015) 121.
7. Y.F. Chen, M. Liu, X.Q. Zeng and W.J. Ding, *Mater. Corros.*, 66 (2015) 949.
8. A. Stenta, S. Basco, A. Smith, C. Clemons, D. Golovaty, K. L. Kreider, J. Wilder, G. W. Young and R. S. Lillard, *Corros. Sci.*, 88 (2014) 36.
9. K.B. Deshpande, *Corros. Sci.*, 62 (2012) 184.
10. J.X. Jia, G.L. Song and A. Atrens, *Adv. Eng. Mater.*, 9 (2007) 65.
11. J.X. Jia, G.L. Song and A. Atrens, *Corros. Sci.*, 48 (2006) 2133.
12. C.H. Sun, Y. Tan, K. He, S.H. Zhang, K.X. Liang and Q. Lu, *Int. J. Electrochem. Sci.*, 15 (2020) 3298.
13. X.D. Zhang, X.Q. Du, S. Feng and Z. Zhang, *Int. J. Electrochem. Sci.*, 13 (2018) 4911.
14. J.X. Jia, G.L. Song and A. Atrens, *Mater. Corros.*, 56 (2005) 259.
15. J.X. Jia, A. Atrens, G.L. Song and T.H. Muster, *Mater. Corros.*, 56 (2005) 468.
16. G.L. Song, B. Johannesson, S. Hapugoda and D. StJohn, *Corros. Sci.*, 46 (2004) 955.
17. Z.M. Shi, J.X. Jia and A. Atrens, *Corros. Sci.*, 60 (2012) 296.
18. K.B. Deshpande, *Corros. Sci.*, 52 (2010) 2819.
19. A.D. King, J. S. Lee and J.R. Scully, *J. Electrochem. Soc.*, 163 (2016) C342.
20. R. Sánchez-Tovar, M.T. Montañés and J. García-Antón, *Corros. Sci.*, 68 (2013) 91.
21. C.L. Wang, Q.F. Li and J.H. Wang, *Key Eng. Mater.*, 525-526 (2013) 325.

22. E. Blasco-Tamarit, A. Igual-Muñoz, J. García Antón and D. García-García, *Corros. Sci.*, 49 (2007) 1000.
23. I. Nakatsugawa and Y. Chino, *Mater Trans.*, 62 (2021) 1764.
24. I. Nakatsugawa and Y. Chino, *J. Electrochem. Soc.*, 167 (2020), 061501.
25. A.I. Ikeuba, B. Zhang, J.Q. Wang, E.H. Han and W. Ke, *J. Mater. Sci. Technol.*, 35 (2019) 1444.
26. F. Thébault, B. Vuillemin, R. Oltra, C. Allely and K. Ogle, *Electrochim. Acta*, 82 (2012) 349.
27. J. Izquierdo, L. Nagy, S. González, J.J. Santana, G. Nagy and R.M.Souto, *Electrochem. Commun.*, 27 (2013) 50.
28. D. Mizuno and R.G. Kelly, *Corrosion*, 69 (2013) 580.
29. C. Huang, F. Huang, H.X. Liu, Q. Hu and J. Liu, *Corros. Eng. Sci. Techn.*, 54 (2019) 556.
30. D. Filotás, B.M. Fernández-Pérez, J. Izquierdo, A. Kiss, L. Nagy, G.Nagy and R.M. Souto, *Corros. Sci.*, 129 (2017) 136.
31. X. Joseph Raj and T. Nishimura, *J. Ind. Eng. Chem.*, 41 (2016) 141.
32. S. Miyabe; N. Fujii and S. Fujimoto, *Mater Trans.*, 62 (2021) 1489.
33. A. Mohammadian, R. Rashetnia, G. Lucier, R. Seracino and M. Pour-Ghaz, *Cement Concrete Comp.*, 103 (2019) 263.
34. A. Ruiz-Garcia, R. Mayen-Mondragon, J. Genesca, E. Morales-Murillo, J. Taha-Tijerina and R. Montoya, *Mater. Corros.*, 71 (2020) 401.
35. H.X. Lin, C. Zhang, Y.M. Huang, R. Zhao and L.X. Yang, *IEEE Wirel. Commun. Lett.*, 11 (2022) 235.
36. A. Anwar, W.Y. Lin, X.K. Deng, J.B. Qiu and H.J. Gao, *IEEE T. Ind. Electron.*, 66 (2019) 8214.
37. S. Palani, T. Hack, J. Deconinck and H. Lohner, *Corros. Sci.*, 78 (2014) 89.
38. Y.L. Chen, H.L. Huang, Y. Zhang, C.G. Wang and W.J. Fan, *Mater. Corros.*, 70 (2019) 79.
39. Q. Hu, Y. Liu, T. Zhang and F. Wang, *Eng. Fail. Anal.*, 109 (2020), 104276.
40. Y. Zhang, Y. Chen, W. Fan, C. Wang and G. Bian, *Mater. Corros.*, 68 (2017) 1107.
41. C. Thiel, C. Broecheler, F. Ludwar, A. Rennings, J. Doose and D. Erni, *J. Mar. Sci. Eng.*, 8 (2020) 105.
42. M.S. Hong, Y.S. Jeon, W.C. Kim, J.C. Jeong and J.G. Kim, *Int. J. Electrochem. Sci.*, 15 (2020) 7013.
43. T. Huber and Y. Wang, *Corrosion*, 68 (2012) 441.
44. G. Song, *Corrosion and Protection of Magnesium Alloy*, Chemical industry press, (2006) Beijing, China.
45. W.Y. Yang, Z.Q. Liu and H.L. Huang, *Corros. Sci.*, 188 (2021), 109562.
46. S. Thomas, N.V. Medhekar, G.S. Frankel and N. Birbilis, *Solid State Mater. Sci.*, 19 (2015) 85–94.
47. L. Wang, T. Shinohara and B.P. Zhang, *Zairyo to Kankyo*, 58 (2009) 105–110.
48. Y. Liu, X. Liu, Z.C. Zhang, N. Farrelld, D.F. Chen and Y.F. Zheng, *Corros. Sci.*, 161 (2019), 108185.
49. G. Song and A. Atrens, *Adv. Eng. Mater.*, 5 (2003) 837.
50. N. Zidane, Y. Ait Albrimi, A. Ait Addi, J. Douch, R.M. Souto and M. Hamdani, *Int. J. Electrochem. Sci.*, 13 (2018) 29.
51. A. Pardo, P. Casajus, M. Mohedano, A.E. Coy, F. Viejo, B. Torres and E. Matykina, *Appl. Surf. Sci.*, 255 (2009) 6968.
52. D. Hoche, *J. Electrochem. Soc.*, 162 (2015) C1.
53. L.H. Yang, C.G. Lin, H.P. Gao, W.C. Xu, Y.T. Li, B.R. Hou and Y.L. Huang, *Int. J. Electrochem. Sci.*, 13 (2018) 8084.
54. K. Xiao, C.F. Dong, D. Wei, J.S. Wu and X.G. Li, *J. Wuhan Univ. Technol. Mater. Sci.*, 31 (2016) 204.